Large eddy simulation of fiber flocculation in a diffuser: Effects of fiber inertia and reinjection kinematics

International Journal of Multiphase Flow 197 (2026) 105627

Contents lists available at ScienceDirect

International Journal of Multiphase Flow

journal homepage: www.elsevier.com/locate/ijmulflow

Research Paper

Large eddy simulation of fiber flocculation in a diffuser: Effects of fiber inertia and reinjection kinematics

MohammadJavad Norouzi [a,*], Jelena Andrić [b], Anton Vernet [a], Jordi Pallares [a], Håkan Nilsson [c]

[a] Department d'Enginyeria Mecànica, Universitat Rovira i Virgili, Països Catalans, 26, Tarragona, 43007, Spain
[b] Department of Architecture and Civil Engineering, Chalmers University of Technology, Sven Hultins gata 6, Göteborg, 412 96, Sweden
[c] Department of Mechanics and Maritime Sciences, Chalmers University of Technology, Chalmersplatsen 1, Göteborg, 412 96, Sweden

ARTICLE INFO

Keywords:
Fiber suspension
Flocculation
Particle-level simulation
Diffuser
Ballistic deflection
Large eddy simulation

ABSTRACT

This study investigates flocculation in dilute suspensions of rigid fibers flowing through an asymmetric diffuser using an Eulerian–Lagrangian approach. The analysis focuses on flow-induced ballistic flocculation under varying fiber inertia and inlet (reinjection) kinematics. The fiber length exceeds the Kolmogorov length scale of the carrier flow, and finite inertia leads to a non-negligible slip velocity relative to the fluid. Large eddy simulation (LES) is applied with a dynamic subgrid-scale model to resolve the flow field and turbulence. One-way coupling between the fibers and the flow is assumed, while fiber–fiber interactions are modeled using short-range attractive forces that promote floc formation. The results show that ballistic deflection significantly accelerates flocculation in the diffuser region, establishing ballistic deflection as the dominant mechanism. In addition, inlet fiber kinematics and inertia strongly influence flocculation within the straight inflow channel.

1. Introduction

Understanding the dynamics of inertial anisotropic particles in turbulent flows is a fundamental issue in multiphase flows, with significant relevance across various fields, from papermaking (Lundell et al., 2011) to cloud ice-crystal formation (Sherwood et al., 2006) to locomotion of microorganisms (Saintillan and Shelley, 2007; Locsei and Pedley, 2009; Parsa et al., 2012). Industries such as pulp and paper processing and composites production rely on achieving a uniform spatial distribution of fibers to ensure the quality of their end products (Norouzi et al., 2022; Martínez et al., 2020). Consequently, the formation of fiber flocs is highly undesirable in these contexts, highlighting the need to disrupt or prevent their formation. In contrast, in wastewater and drinking water treatment and physical filtration, the aggregation of suspended solids is a desired process. Therefore, a thorough understanding of the complex interactions between fibers and flows is necessary to accurately predict and control flocculation in flowing suspensions (Andrić et al., 2016).

The interaction between non-spherical particles and turbulent flow is highly complex. In addition to the complexities introduced by turbulence in flows with spherical particles, forces and torques dependent on particle shape and orientation must also be considered (Voth and Soldati, 2017; Marchioli and Soldati, 2013). A comprehensive review of the numerical models available to characterize the translation and rotation of non-spherical particles in fluid flows was presented by Voth and Soldati (2017). To examine particle–turbulence interactions at the particle scale, it is common to combine an Eulerian description of the carrier flow with a Lagrangian description of the particles (Toschi and Bodenschatz, 2009). When the particle Reynolds number is significantly smaller than unity and the particle Stokes number is small, the translational and rotational slip are negligible and particles can be assumed to act as perfect flow tracers (Dotto and Marchioli, 2019). Exact equations governing the evolution of particle orientation exist for both axisymmetric (Jeffery, 1922) and non-axisymmetric particles (Hinch and Leal, 1979), providing valuable insight into the motion of elongated micro-swimmers and non-motile plankton cells in turbulent environments (Lovecchio et al., 2017, 2013; Ardekani et al., 2017). However, when particle–fluid relative motion cannot be disregarded, rigid body motion equations should be employed (Zhao et al., 2014; Dotto and Marchioli, 2019), as employed in studying rigid ellipsoid motion in both viscous and turbulent flows (Challabotla et al., 2015; Marchioli and Soldati, 2013; Marchioli et al., 2010; Zhao et al., 2019b, 2015).

Most of studies concerned with the motion of rigid non-spherical particles in turbulence (Zhao and Andersson, 2020; Zhao et al., 2019a;

* Corresponding author.
E-mail addresses: norouzi.mohammadjavad@gmail.com (M. Norouzi), jelena.andric@chalmers.se (J. Andrić), anton.vernet@urv.cat (A. Vernet), jordi.pallares@urv.cat (J. Pallares), hakan.nilsson@chalmers.se (H. Nilsson).

https://doi.org/10.1016/j.ijmultiphaseflow.2026.105627
Received 4 April 2025; Received in revised form 25 December 2025; Accepted 19 January 2026
Available online 20 January 2026

Ardekani and Brandt, 2019) highlight the particles' tendency to align with the direction of the strongest Lagrangian fluid stretching (Zhao and Andersson, 2020; Ni et al., 2014). As the particle Reynolds number reaches unity or higher, the combined impact of fluid and particle inertia must be considered (Lopez and Guazzelli, 2017). Furthermore, particle shape and size have been shown to affect inertia-driven phenomena such as preferential concentration and near-wall accumulation (Marchioli and Soldati, 2013; Zhao et al., 2019a; Marchioli et al., 2010; Njobuenwu and Fairweather, 2016).

Numerous studies have examined the impact of fiber and flow properties, as well as fiber concentration on the phenomenon of fiber flocculation. Schmid et al. (2000) analyzed the effect of attractive and frictional forces on fiber aggregation and reported that fiber flocculation can be induced solely by inter-fiber friction, even in the absence of attractive forces. Switzer III and Klingenberg (2003) demonstrated the importance of fiber shape and deformability on their flocculation. Kerekes and Schell (1995) studied fiber flocculation in dilute suspensions and showed that increased contact area and entanglement between longer fibers promote the formation of larger and more stable flocs. Fiber rotation not only directly impacts the behavior of individual particles by affecting drag forces (Meyer et al., 2013) but also determines whether two particles in close proximity will collide or avoid each other (Koch and Shaqfeh, 1989). The frequency of fiber–fiber collisions depends on the relative motion and local concentration; higher concentrations increase encounter probability and are associated with greater flocculation (Schmid et al., 2000; Switzer III and Klingenberg, 2003). Moreover, when fiber trajectories significantly deviate from the flow streamlines, the fibers have an increased probability of crossing each other and forming flocs (Andric et al., 2017; Andrić et al., 2016, 2013). Jafari et al. (2006) investigated the influence of contact and lubrication forces on floc formation and breakup of fibers in turbulent channel flow, observing the fibers' tendency to accumulate in high-speed streaks in the near-wall regions. Njobuenwu and Fairweather (2016) observed similar phenomena and reported that the translational dynamics of fibers, in terms of preferential concentration, are strongly dependent on their inertia and less dependent on their aspect ratio. Fiber-level simulations have demonstrated their efficacy in analyzing small-scale geometries containing up to 10^4 particles (Hämäläinen et al., 2011). However, to tackle larger flow geometries, Hämäläinen et al. (2011) employed a Fiber Floc Evolution Model (FFEM) based on the integration of the population balance method and an Eulerian two-fluid approach, which elucidated that the size distribution of flocs is strongly influenced by local flow conditions.

Andrić et al. (2016) studied the motion of rod-like fibers in the decelerating flow of a wedge-shaped channel using analytical and numerical methods, considering both infinite and finite hydrodynamic resistance to transverse flow. They identified the phenomenon of ballistic deflection, where fiber trajectories deviate significantly from the streamlines of the carrying flow. This phenomenon occurs when the direction of fiber inertia is aligned with converging/diverging or curved streamlines. A velocity difference between the fibers and the fluid develops due to fiber inertia and the gradients of the flow. For elongated fibers with an anisotropic hydrodynamic resistance tensor, this velocity difference is predominantly oriented in the longitudinal direction of the fiber. Andrić et al. (2016) argued that ballistic deflection increases the relative motion of fibers, which may increase the collision rate and thus affect the rate of aggregation. In a subsequent study, Andric et al. (2017) examined the flocculation of suspensions of rigid fibers in the decelerating flow field of a diffuser. They modeled the fibers using a particle-level fiber model and described the fluid flow using the two-dimensional steady-state Navier–Stokes equation with the standard $k-\omega$ turbulence model to account for the effects of turbulence, as well as a stochastic model to include the dispersion of fibers due to turbulence. The main finding of their study was that the anisotropic hydrodynamic resistance of fibers and the flow velocity gradients induce ballistic deflection of fibers, consequently causing fiber flocculation in the diffuser. They also observed that the kinematics of reinjected fibers strongly affect the flocculation in the horizontal inflow channel and at the entrance of the diffuser.

To the best of the authors' knowledge, no study has analyzed fiber suspensions in an asymmetric diffuser using Large Eddy Simulation (LES) to resolve both the flow and the fiber-flow interaction in detail. In an effort to address this limitation, the present study builds upon the work of Andric et al. (2017) and provides a comprehensive investigation on the evolution of floc mass fraction, fiber trajectories, fiber slip velocities, alignment of fibers with respect to the inertial coordinate, to examine the development of fiber flocculation along the length of the diffuser. Specifically, the phenomenon of flow-induced ballistic flocculation, triggered by ballistic deflection of fibers, is analyzed for fibers with different inertia (controlled by varying the fiber density) and various fiber reinjection approaches (adjusting the orientation, linear, and angular velocity of the fibers upon their reinjection into the computational domain).

2. General overview of case study

A fiber suspension flow in an asymmetric planar diffuser is considered, as illustrated in Fig. 1. The highlighted region indicates where the fibers are present, while the elongated inlet and outlet regions (truncated in the figure) ensure that the fiber interactions are unaffected by inlet and outlet effects. This specific configuration has been chosen as it accurately represents the flow conditions encountered in the actual dry-forming process (Andric et al., 2017), and a robust experimental database is available for validating the simulated flow (Obi et al., 1993; Buice and Eaton, 2000). A Cartesian coordinate system is used, with the origin located at the lower wall at the start of the expansion. The x-axis corresponds to the streamwise direction, the y-axis represents the upward direction, and the z-axis denotes the spanwise direction. Unless stated otherwise, spatial coordinates are non-dimensionalized by the inlet height H, *i.e.,* reported as x/H and y/H.

Fibers advected through $x = 36H$ are reinjected as isolated fibers with a uniform random spatial distribution at the inlet plane $x = -15H$. The reinjection procedure for fibers that contact a wall is chosen intentionally as a simple, physically motivated, modeling approach. Fibers that contact a wall are assumed to adhere either to the solid surface or to previously adhered fibers without affecting the properties of the wall, and do not interact with the flocculation in the downstream flow. This assumption reduces the downstream fiber concentration—a physically consistent outcome when a fraction of fibers becomes attached to the walls. Since the fibers adhering to the walls do not interact with other fibers, they are reinjected at the inlet to conserve the global particle count. This choice intentionally avoids modeling long-term wall evolution (surface roughening, bed porosity, re-entrainment, time-dependent adhesion), which would require additional contact and adhesion physics and would change the scope of the present study. Flocs are treated as intact aggregates; if any member of a floc contacts a wall, the entire floc is removed and all constituent fibers are reinjected individually at the inlet plane following the same procedure as for single fibers. The fiber motion is periodic in the z-direction, which means that fibers or flocs advected through the plane at $z = H$ or the plane at $z = -H$ are repositioned in the opposite plane while retaining their properties.

3. Fiber suspension modeling

This study employs a Lagrangian fiber model to represent the fibers, combined with Large Eddy Simulation (LES) equations to describe the behavior of the fluid flow. Within this model, a one-way interaction approach is used to account for the influence of fluid flow on the fibers, and a contact model is incorporated to capture interactions among fibers. The following subsections provide an overview of the fluid flow model, the fiber model, the fluid-fiber and fiber–fiber interaction approaches, and the fiber reinjection approaches used in this work.

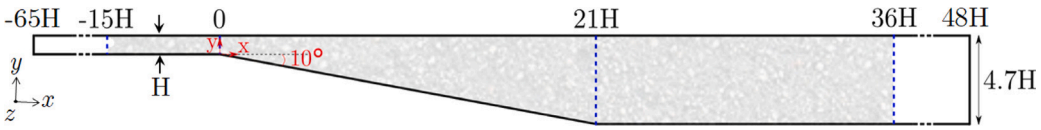

Fig. 1. Schematic of Buice and Eaton asymmetric diffuser (Buice and Eaton, 2000). The highlighted region denotes where the fibers are present. The inlet and outlet regions are truncated for clarity. The flow computational domain extends from $z = -2H$ to $z = 2H$ in the spanwise direction, where $H = 0.01\text{m}$ is the inlet height.

3.1. Fluid flow model

The Large Eddy Simulation (LES) approach for incompressible flows is based on the filtered continuity and momentum equations obtained by applying a spatial filter of scale Δ to the Navier–Stokes equations. The resulting equations are given by

$$\frac{\partial \bar{u}_i}{\partial x_i} = 0, \tag{1}$$

$$\frac{\partial \bar{u}_i}{\partial t} + \frac{\partial (\bar{u}_i \bar{u}_j)}{\partial x_j} = -\frac{1}{\rho}\frac{\partial \bar{p}}{\partial x_i} + \nu \frac{\partial^2 \bar{u}_i}{\partial x_j \partial x_j} - \frac{\partial \tau_{ij}}{\partial x_j}. \tag{2}$$

Here t denotes time, x_j is the spatial coordinate directions, u_j is the velocity vector, p is the pressure, ν is the fluid kinematic viscosity, and $\tau_{ij} = \overline{u_i u_j} - \bar{u}_i \bar{u}_j$ is the Sub-Grid Scale (SGS) tensor which represents the effect of the SGS motions on the resolved motions. The SGS stress τ_{ij} is modeled analogously to the Boussinesq hypothesis, yielding

$$-\frac{\partial \tau^a_{ij}}{\partial x_i} \equiv \frac{\partial}{\partial x_i}(2\nu_{sgs}\bar{S}_{ij}). \tag{3}$$

Here τ^a_{ij} is the anisotropic part of the SGS tensor, $\bar{S}_{ij} = \frac{1}{2}\left(\frac{\partial \bar{u}_i}{\partial x_j} + \frac{\partial \bar{u}_j}{\partial x_i}\right)$ is the filtered strain rate tensor, and the coefficient of proportionality ν_{sgs} represents the SGS viscosity that should be determined using an SGS model. Among existing SGS models, the dynamic one-equation eddy viscosity model is used in the present work. This model is a modified form of the standard one-equation model, where the SGS kinetic energy production term is resolved by applying an SGS model based on resolved scales (Kajishima and Nomachi, 2006), while the eddy viscosity in the filtered equation of motion is computed using information derived from unresolved scales in the transport equation of the SGS kinetic energy. For an in-depth description of the SGS model employed here, the readers are encouraged to refer to Kajishima and Nomachi (2006), Yoshizawa and Horiuti (1985), Horiuti (1985), Okamoto and Shima (1999), Tang et al. (2019).

The governing equations are solved numerically using the OpenFOAM open-source CFD code (Weller et al., 1998) with the pimpleFoam solver. This solver combines the functionalities of the PISO (Pressure-Implicit with Splitting of Operators) and the SIMPLE (Semi-Implicit Method for Pressure-Linked Equations) algorithms. To ensure accuracy, the advection terms are discretized using a second-order upwind scheme, while the implicit backward Euler scheme is used to discretize the unsteady terms.

The inlet boundary of the fluid flow specifies a constant bulk velocity of $U_b = 28$ m/s. The flow passes through a $50H$ upstream section before reaching the fiber region at $x = -15H$, ensuring that it is fully developed upon entry. At the outlet, at $x = 48H$, a zero gradient condition is applied, while a no-slip boundary condition is applied to the top and bottom walls of the channel. The computational mesh comprises $1020 \times 120 \times 64$ cells and is appropriately refined to capture gradients near the wall. The measured skin friction coefficient, C_f, in the fully developed entrance region is 0.0061, and the first cell centers are typically located at $y^+ \approx 1$.

3.2. Fiber model

The particle-level fiber model used in this work is based on the model proposed by Lindström and Uesaka (2007) and Andrić et al. (2013), specialized for rigid straight fibers as employed by Andric et al. (2017). Readers are referred to these references for a detailed description of the model. In the interest of completeness, only the key characteristics of the model will be highlighted here.

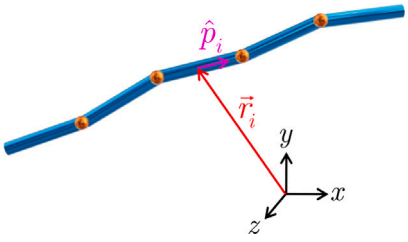

Fig. 2. Illustration of a general non-straight fiber to highlight the segments. This study focuses solely on straight rigid fibers.

To accommodate the variations in the flow field along the length of the fiber, the suspended fiber is treated as a chain of $N_{seg} = 5$ cylindrical segments, as illustrated in Fig. 2 (only shown non-straight to highlight the segments). Each segment has identical mass m_i, length l_i, diameter d_i, and a unit orientation vector denoted as $\vec{p}_i$, with subscript i indicating individual segments. The center of mass of each segment is located at position vector $\vec{r}_i$, while the fiber's center of mass is given by $\vec{r}_G = \frac{1}{N_{seg}}\sum_{i=1}^{N_{seg}} \vec{r}_i$. Moreover, since the fiber is rigid, each segment has the same angular velocity as the fiber center of mass ($\vec{\omega}_i = \vec{\omega}_G$). The fiber motion is governed by Euler's first and second law, formulated as (Andrić et al., 2016)

$$m\ddot{\vec{r}}_G = \sum_{i=1}^{N_{\text{seg}}} \vec{F}^h_i \tag{4}$$

$$\frac{\mathrm{d}}{\mathrm{d}t}\left(\bar{\bar{I}}_G \cdot \vec{\omega}\right) = \bar{\bar{I}}_G \cdot \dot{\vec{\omega}} + \vec{\omega} \times \left(\bar{\bar{I}}_G \cdot \vec{\omega}\right) = \sum_{i=1}^{N_{seg}} \vec{T}^h_i + \sum_{i=1}^{N_{seg}} \left(\vec{r}_i - \vec{r}_G\right) \times \vec{F}^h_i. \tag{5}$$

Here $\vec{F}^h_i$ and $\vec{T}^h_i$ are the hydrodynamic drag force and torque exerted by the fluid on segment i, and $\bar{\bar{I}}_G$ is the inertia tensor of the fiber with respect to its center of mass.

3.3. Fluid-fiber interactions

In the present work, fluid-fiber interactions are modeled using a one-way coupling approach, a reasonable simplification which allows one to isolate and characterize particle-level ballistic and collision mechanisms. This assumption is quantitatively justified by the extremely dilute nature of the suspension. For the densest configuration considered (see Section 4), the particle volume fraction is $\alpha = V_p/V_f \approx 9\times10^{-6}$ and mass loading (fiber-to-fluid mass ratio) is $\approx 2\%$, well inside the dilute regime where particle back-reaction on the flow is expected to be negligible (Elghobashi, 1994; Tom and Bragg, 2019; Olivieri et al., 2022).

The fiber Reynolds number is defined as

$$Re_f = \frac{d|\vec{r}_G - \vec{v}_G|}{\nu}, \tag{6}$$

where d is fiber diameter, ν is the kinematic viscosity of the fluid, and $|\dot{\vec{r}}_G - \vec{v}_G|$ is the magnitude of the relative velocity between the fiber and the flow at the center of mass of the fiber. According to Lindström and Uesaka (2007), the hydrodynamic force ($\vec{F}_i^h$) and the hydrodynamic torque ($\vec{T}_i^h$) can be approximated as a sum of viscous ($Re_f \ll 1$) and dynamic drag ($Re_f \gg 1$) contributions, *i.e.,*

$$\vec{F}_i^h = \vec{F}_i^{h,V} + \vec{F}_i^{h,I}, \tag{7}$$

$$\vec{T}_i^h = \vec{T}_i^{h,V} + \vec{T}_i^{h,I}. \tag{8}$$

Here the viscous drag force $\vec{F}_i^{h,V}$ and torque $\vec{T}_i^{h,V}$ on each cylindrical segment are approximated as those acting on an isolated equivalent prolate spheroid of aspect ratio $r_e = 1.24 r_f / \sqrt{\ln r_f}$ through

$$\vec{F}_i^V = \bar{\bar{A}}_i^V \cdot \left(\vec{v}_i - \dot{\vec{r}}_i\right), \tag{9}$$

$$\vec{T}_i^V = \bar{\bar{C}}_i^V \cdot \left(\vec{\Omega}_i - \vec{\omega}_i\right) + \bar{\bar{H}}_i^V : \bar{\bar{E}}. \tag{10}$$

Here $\bar{\bar{A}}_i^V$, $\bar{\bar{C}}_i^V$, and $\bar{\bar{H}}_i^V$ are the resistance tensors that are approximated by the corresponding resistance tensors of a prolate spheroid with an equivalent aspect ratio proposed by Kim and Karrila (2013) and are not reported here for the sake of brevity. The properties $\vec{v}_i$, $\vec{\Omega}_i = \frac{1}{2}\left(\nabla \times \vec{v}_i\right)$ and $\bar{\bar{E}} = \frac{1}{2}\left(\nabla \vec{v}_i + \left(\nabla \vec{v}_i\right)^t\right)$ are, respectively, the translational fluid velocity, the angular fluid velocity, and the strain rate tensor, all evaluated at the center of mass of each segment i.

The dynamic drag force and torque on each fiber segment can be computed as (Lindström and Uesaka, 2007)

$$\vec{F}_i^I = \bar{\bar{A}}_i^I \cdot \left(\vec{v}_i - \dot{\vec{r}}_i\right), \tag{11}$$

$$\vec{T}_i^I = \bar{\bar{C}}_i^I \cdot \left(\vec{\Omega}_i - \vec{\omega}_i\right) + \bar{\bar{H}}_i^I : \bar{\bar{E}}, \tag{12}$$

where the dynamic resistance tensors $\bar{\bar{A}}_i^I$, $\bar{\bar{C}}_i^I$, and $\bar{\bar{H}}_i^I$ are derived and validated by Lindström and Uesaka (2007) and Andrić et al. (2013).

3.4. Fiber–fiber interactions

Fiber contacts are detected using the shortest distance algorithm, as detailed by Schmid et al. (2000), Lindström and Uesaka (2007) and Vega and Lago (1994), not repeated here for brevity. Fibers are treated either as isolated rigid bodies or as constituents of rigid flocs. The flocculation model used follows the approach of Andric et al. (2017): whenever two segments belonging to different fibers or flocs come into contact, they are assumed to stick irreversibly, and the resulting aggregate is advanced as a single rigid body with no slippage, internal relative motion or flexibility. The floc preserves fixed relative positions and orientations of its constituent segments and the hydrodynamic forces and torques on a floc are obtained by summing the segment-wise contributions (Eqs. (7)–(12)) over all constituent segments. This superposition is consistent with the present resistance-based, one-way-coupled closure, while neglecting intra-floc hydrodynamic interactions (*e.g.,* shielding/wake overlap). The equations of motion for fibers and flocs are discretized in time and solved to obtain linear and angular velocities, which are then used to update positions and orientations (see Andrić et al. (2013), Andric et al. (2017) for numerical details and timestep considerations). The employed rigid-floc approximation is a conservative, mechanistic idealization of early-stage aggregation; it isolates the hydrodynamic driver (flow deceleration and particle inertia, as discussed later in Section 5.2) that promotes contacts while avoiding additional, uncertain parameters (such as bond strength, sliding friction, breakage criteria) that lie outside the scope of the present study.

3.5. Fiber reinjection approaches

Fiber reinjection is performed at the fiber reinjection plane $x = -15H$ with a random spatial distribution. The relatively long distance between the fiber reinjection plane and the diffuser entry provides reinjected fibers with sufficient upstream distance to adapt to the carrier flow before entering the diffuser. For the suspension properties reported in Section 4.1, the single-response length $L_{\mathrm{resp}} \approx U_{\mathrm{b}} \tau_p$, where $\tau_p \approx \rho_p d^2/(18\,\mu)$ is the particle relaxation time (neglecting slender-body prefactors and rotational/translational coupling), μ is the fluid dynamic viscosity, ranges from $\sim 0.005H$ for the lightest particles to $\sim 10H$ for the heaviest particles; consequently, fibers undergo on the order of at least one response time to relax. The linear velocity, angular velocity, and orientation of reinjected fibers influence their initial trajectories, and hence the initial flocculation rate. The effects of these properties on the flocculation rate are therefore parametrically studied as a part of the present work.

3.5.1. Orientation

In this study, fibers are reinjected using three different orientation approaches ($\vec{p}_{\mathrm{reinj}}$): aligned with the x-axis, aligned with the y-axis, or with a random initial orientation.

3.5.2. Linear velocity

The linear velocity of each fiber segment should correspond to the background flow. However, due to the fiber inertia a reinjected fiber segment should not necessarily be given the same velocity as the instantaneous background flow. A temporary background flow velocity peak may introduce an unreasonable reinjection velocity. The mean flow velocity may thus be a better alternative for the reinjection velocity. A parameter k is introduced to distinguish the chosen background velocity, as

$$\vec{v}_i = (1-k)\vec{U}_{\mathrm{mean}} + k\vec{U}_{\mathrm{inst}}, \tag{13}$$

where $k = 1$ represents the instantaneous flow field ($\vec{U}_{\mathrm{inst}}$) and $k = 0$ represents the time-averaged velocity field ($\vec{U}_{\mathrm{mean}}$). To determine the linear velocity of each fiber segment upon reinjection, first it is assumed that the entire fiber is at mechanical equilibrium with the chosen background flow, *i.e.,* the net forces acting on the particle is zero ($\sum_{i=1}^{N_{seg}} \vec{F}_i = \vec{0}$). Under this assumption and considering only the viscous part of the fiber drag force in Eq. (4), the linear velocity of the fiber center of mass can be computed by averaging the fluid velocity (instantaneous or time-averaged) at the positions of the fiber segments as

$$\dot{\vec{r}}_G = \frac{\sum_{i=1}^{N_{seg}} \vec{v}_i}{N_{seg}}. \tag{14}$$

As the fiber is a rigid body, the reinjection velocity of each segment is given by

$$\vec{u}_{reinj_i} = \dot{\vec{r}}_G + \frac{\sum_{i=1}^{N_{seg}} -\frac{\left(\vec{v}_i - \dot{\vec{r}}_G\right)\times\left(\vec{r}_i - \vec{r}_G\right)}{\left\|\vec{r}_i - \vec{r}_G\right\|}}{N_{seg}} \times \left(\vec{r}_i - \vec{r}_G\right). \tag{15}$$

3.5.3. Angular velocity

The angular velocity of a fiber upon reinjection is set under the assumption of rotational equilibrium with the flow, implying zero net moment (*i.e.,* $\sum_{i=1}^{N_{seg}} \vec{T}_i = \vec{0}$). Applying this assumption to Eq. (5), an equation to $\vec{\omega}_{reinj}$ can be derived as

$$\vec{\omega}_{reinj} = \frac{\sum_{i=1}^{N_{seg}} \vec{\Omega}_i - \sum_{i=1}^{N_{seg}} \left(\bar{\bar{H}}_i^V : \bar{\bar{E}}\right) \cdot \left(\bar{\bar{C}}_i^V\right)^{-1}}{N_{seg}}. \tag{16}$$

4. Specification of studied cases

This section provides details on the studied cases, including fluid and fiber properties, the initialization process using a precursor simulation, and the specific simulation cases along with their investigated parameters.

4.1. Fluid and fiber properties

The carrier fluid is considered to be air, characterized by a density of $\rho = 1.2$ kg/m^3 and kinematic viscosity of $\nu = 1.4 \times 10^{-5}$ m^2/s, corresponding to a Reynolds number of $\mathrm{Re} = \frac{U_b H}{\nu} = 18000$ at the inlet boundary. The Kolmogorov length estimated from crude scaling $\varepsilon \sim U_b^3/H$ is $\eta_K = (\nu^3/\varepsilon)^{1/4} \approx 6$ μm. Based on the LES velocity field, the streamwise turbulence intensity is $u_x'/U_b \approx 0.1$. Thus, $\varepsilon \sim U_b^3/H$ should be regarded as a crude upper bound for ε and, consequently, a conservative lower bound for η_K; accordingly, $\eta_K = \mathcal{O}(10\ \mu\mathrm{m})$. The smallest LES wall-normal spacing is $\Delta y_1 \approx 9.1$ μm and representative filter widths in the fiber region are of the order of $\mathcal{O}(10-10^2\ \mu\mathrm{m})$.

Each fiber is assumed to consist of five segments with a diameter of $d = 20$ μm and a length of $l = 0.2$ mm. The study examines a range of fiber densities $\left[\rho_{ref}/1000 \text{ - } 2\rho_{ref}\right]$ kg/m^3, with a reference density of $\rho_{ref} = 1380$ kg/m^3, providing an analysis of the influence of varying fiber inertia on fiber flocculation.

Rigid straight fibers experience total hydrodynamic force and torque given by the sum of the local forces and torques exerted on each segment. In the present study the modeled fiber geometry is $d \approx 3.4\,\eta_K$, $l \approx 33.6\,\eta_K$ and $L_{\mathrm{fib}} = N_{\mathrm{seg}} \times l \approx 168\,\eta_K$; hence the LES grid and filter resolve flow features at scales comparable to the fiber diameter and segment length (*i.e.,* larger than the Kolmogorov scale). The resolved-field variability that drives ballistic deflection is therefore captured at meso- and geometry-scales (resolved variability ~10 μm to 100 μm), and our 200 μm sampling interval provides a smooth, faithful representation of the resolved velocity and strain fields. Dissipative, sub-η_K motions are treated implicitly by the SGS closure rather than being directly resolved. The employed rod-chain model of Lindström and Uesaka (2007) and Andrić et al. (2013) assembles per-segment resistances into net rigid-body forces and torques. For smooth resolved fields, only a modest number of segments is required to obtain accurate integrated forces and torques. Using five segments introduces negligible hydrodynamic error while substantially lowering per-particle cost, which scales approximately linearly with segment count (Andric et al., 2017; Andrić et al., 2016; Schmid et al., 2000; Switzer and Klingenberg, 2004; Switzer III and Klingenberg, 2003).

4.2. Precursor simulation

A precursor fiber simulation was initiated when a fully developed fluid flow was established. A total of 3000 fibers were initially distributed randomly within the range $\{[-15H, 36H], [0, H], [-H, H]\}$ in the x, y, and z directions, respectively, as done by Andric et al. (2017). The initial translational and angular velocities of the fibers were set equal to those of the fluid flow at the center of mass of each fiber. A fully developed fiber flow was established after seven complete reinjections of all fibers. The configuration of fiber segments and their kinematics from the precursor fiber simulation were saved and later used as the reference time zero for the parametric studies, ensuring that all simulations had the same initial conditions. Fig. 3 shows a snapshot taken at time zero, illustrating the distribution of fibers and flocs in the diffuser, overlaid with velocity magnitude contours. The fiber dimensions are scaled for visibility, while the inlet and outlet regions are excluded to provide a focused view of the fiber region.

4.3. Simulation cases and studied parameters

The parametric study investigates the development of fiber flocculation along the diffuser by analyzing the effects of fiber inertia and various reinjection approaches which involve adjusting the fibers' orientation, linear velocity, and angular velocity upon reinjection.

Table 1 summarizes the simulation parameters used to characterize each case of fiber suspension. In Case 1, fibers have a reference density of $\rho_{ref} = 1380$ kg/m^3, and the computational domain for fiber flocculation simulations is restricted to $[-15H, 36H]$ in the longitudinal diffuser direction. The linear velocity of each fiber segment is calculated using Eq. (15) in which the instantaneous fluid velocity field for $k = 1$ in Eq. (13) is considered (denoted as $(u_x, u_y, u_z)|_{k=1}$). The fiber's angular velocity $\vec{\omega}_{reinj}$ is initialized using Eq. (16), and the fiber orientation is assigned randomly. Case 2 differs from Case 1 only in the linear velocity reinjection approach: the longitudinal linear velocity component of each segment is set to the value obtained from Eq. (15) for $k = 0$, *i.e.,* using the time-averaged fluid velocity field $\vec{U}_{\mathrm{mean}}$, while the other two velocity components are set to zero (represented as $(u_x, 0, 0)|_{k=0}$). Cases 3 and 4 share the same properties as Case 2, except for the orientation of the reinjected fibers. Specifically, in Case 3, the fibers are reinjected with an orientation aligned with the streamwise direction (x), while in Case 4, the fibers are oriented in the upward direction (y). Case 5 follows the same reinjection approach as Case 2, but the fiber angular velocity upon reinjection is set to zero. Cases 6 and 9 maintain the same reinjection approach as Case 2 but with fiber densities of $\rho_{\mathrm{ref}}/3$ and $\rho_{\mathrm{ref}}/1000 = 1.38$ kg/m^3 $\approx \rho_{\mathrm{air}}$, respectively. Similarly, Cases 7 and 10 use the same reinjection approach as Case 3, but with different fiber densities. Also, Cases 8 and 11 employ the same reinjection approach as Case 4, but with corresponding variations in fiber density.

5. Results and discussion

This section presents a validation of the fluid flow model and analyzes the fiber flocculation in the diffuser. Additional evaluations of fiber trajectories, slip velocities, and evolution of fiber alignment are conducted to examine the effects of flow parameters and fiber inertia on flocculation.

5.1. Validation of fluid flow model

To validate the fluid flow model utilized in this study, the axial mean velocity and axial Reynolds stress profiles obtained from fully developed simulations are compared to experimental measurements from Buice and Eaton (2000). The axial and vertical positions are normalized by the upstream channel height, H, while the velocity profiles are normalized by the bulk velocity, U_b, and the axial Reynolds stresses are normalized by U_b^2.

Fig. 4(A) shows that the time-averaged streamwise velocity (u_x) profiles of the present LES study accurately agree with the experimental results across all axial locations. Fig. 4(B) compares the numerical and experimental evolutions of the Reynolds stress $\langle u_x' u_x' \rangle$ throughout the diffuser. In general, the LES result tends to slightly underestimate $\langle u_x' u_x' \rangle$ at most locations, but the profiles are similarly shaped as the experimental data. These discrepancies, as suggested by Kaltenbach et al. (1999), may arise from larger experimental errors in turbulent stress measurements relative to mean flow velocities, particularly in regions where measurement volumes are relatively large relative to the local gradients of turbulent stresses. Nevertheless, the authors are confident that the current resolved LES and the dynamic modeling of the SGS term provide a sufficiently accurate representation of the flow field for investigating fiber motion and floc development in the present study.

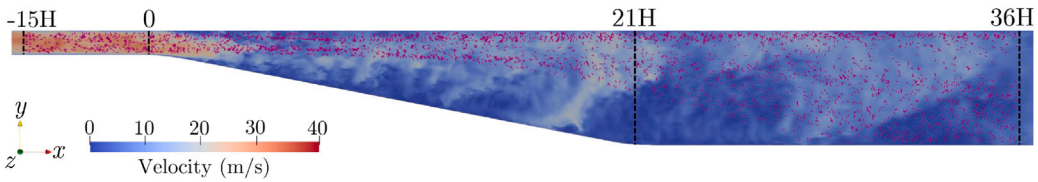

Fig. 3. Distribution of fibers and flocs in the diffuser at the reference time zero, overlaid with the contour of velocity magnitude. The fiber length and diameter are enlarged for visualization purposes. The inlet and outlet regions of the fluid flow are excluded for clarity.

Table 1
Summary of cases and simulation parameters.

Case	ρ (kg/m^3)	k	$\vec{u}_{\text{reinj}}$	$\vec{\omega}_{\text{reinj}}$	$\vec{p}_{\text{reinj}}$	Fiber region (x-dimension)
C1	1380	1	(u_x, u_y, u_z)	(w_x, w_y, w_z)	Random	$[-15H, 36H]$
C2	1380	0	$(u_x, 0, 0)$	(w_x, w_y, w_z)	Random	$[-15H, 36H]$
C3	1380	0	$(u_x, 0, 0)$	(w_x, w_y, w_z)	(1, 0, 0)	$[-15H, 36H]$
C4	1380	0	$(u_x, 0, 0)$	(w_x, w_y, w_z)	(0, 1, 0)	$[-15H, 36H]$
C5	1380	0	$(u_x, 0, 0)$	(0, 0, 0)	Random	$[-15H, 36H]$
C6	460	1	(u_x, u_y, u_z)	(w_x, w_y, w_z)	Random	$[-15H, 36H]$
C7	460	0	$(u_x, 0, 0)$	(w_x, w_y, w_z)	(1, 0, 0)	$[-15H, 36H]$
C8	460	0	$(u_x, 0, 0)$	(w_x, w_y, w_z)	(0, 1, 0)	$[-15H, 36H]$
C9	1.38	1	(u_x, u_y, u_z)	(w_x, w_y, w_z)	Random	$[-15H, 36H]$
C10	1.38	0	$(u_x, 0, 0)$	(w_x, w_y, w_z)	(1, 0, 0)	$[-15H, 36H]$
C11	1.38	0	$(u_x, 0, 0)$	(w_x, w_y, w_z)	(0, 1, 0)	$[-15H, 36H]$

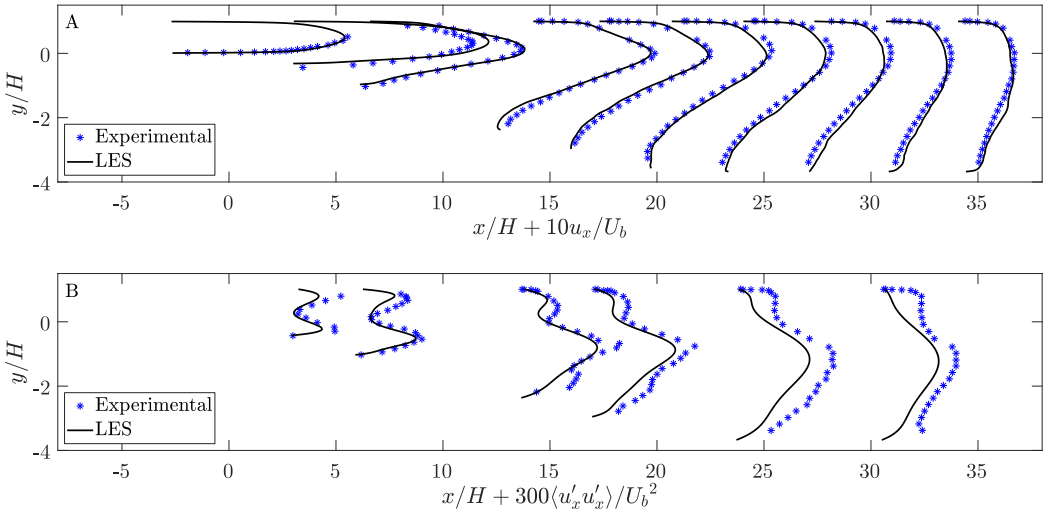

Fig. 4. Development of (A) axial velocity profile and (B) Reynolds stress $\langle u'_x u'_x \rangle$ through the diffuser for the present LES study compared with experimental results of Buice and Eaton (2000).

5.2. Fiber flocculation

At each time step, the interactions between individual fibers and between fibers and flocs are identified, and contacting fibers are merged to form larger flocs, as described in Section 3.4. These flocs are categorized as distinct species denoted by F_i, where i ranges from 1 to n reflecting the number of fibers present in each floc (F_1 corresponds to individual fibers). To examine the distribution of floc species along the diffuser's length, the fiber region is divided into 320 bins of uniform thickness along the streamwise direction for simulation Cases 1–11. The mass fraction of each F_i species in a specific bin is defined as (Andric et al., 2017)

$$\phi_i = \frac{iN_i}{\sum_{k=1}^{n} kN_k}. \tag{17}$$

Here, N_i represents the time-averaged number of flocs belonging to the F_i species in a particular bin. The numerator reflects the time-averaged number of fibers present in flocs consisting of i fibers, while the denominator represents the time-averaged total number of fibers within each bin irrespective of floc size.

This study primarily focuses on the development of the F_2 floc species along the length of the diffuser, due to the limited number of fibers involved and therefore also the limited formation of larger flocs. Additionally, the dimensionless flocculation rate of F_i is given by Andric et al. (2017)

$$\phi_i' = \frac{d\phi_i}{dx} H, \tag{18}$$

where ϕ_i' represents the dimensionless rate of change of the mass fraction F_i species with respect to the streamwise coordinate x, normalized by the diffuser height H.

Fig. 5 illustrates the development of the mass fraction ϕ_2 of floc species F_2 along the length of the diffuser for various reinjection approaches of reference fibers with density of $\rho = 1380$ kg/m^3. It should be recalled that the fibers are reinjected at $x = -15H$, and the fully developed flow in the straight inlet channel section ($-15 < x/H < 0$) fluctuates about a mean flow that is aligned with the channel.

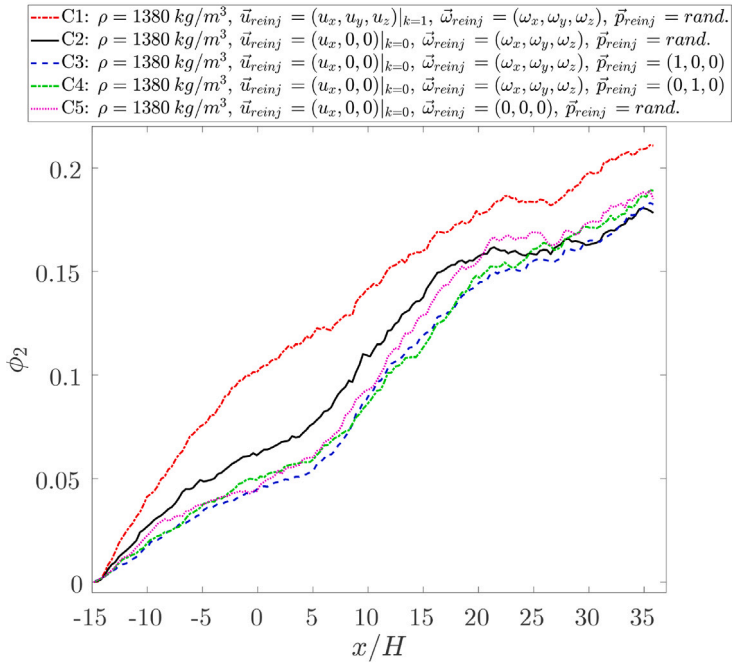

Fig. 5. Development of the mass fraction ϕ_2 of floc species F_2 along the diffuser length for different fiber reinjection approaches.

Under these conditions, an approximately constant initial flocculation rate is expected. However, significant differences in flocculation rates emerge immediately after reinjection, depending on the fiber reinjection approach. Case 1, with reinjection velocities derived from the local instantaneous flow field and random fiber orientations, exhibits the highest initial flocculation rate. For the rest of the cases (*i.e.,* Case 2–5), where the time-averaged fluid velocity field is used to calculate the linear and angular reinjection velocity and then only the streamwise component is taken into account, a lower flocculation rate is observed. Comparing Cases 2 and 3, where fibers are reinjected with flow-aligned orientations, highlights the impact of initial fiber orientation on floc formation in the initial part of the straight inlet channel.

With regard to the development of mass fraction ϕ_2 of Cases 2–5, four regimes can be identified (see Fig. 5). The first regime initiates at the fiber reinjection plane $x/H = -15$ and extends until $x/H \approx -7$ within the straight inlet channel. In this region, an initial rapid increase in floc formation is observed at the very beginning, followed by a nearly linear growth, which reflects a constant rate of flocculation. This part of the diffuser represents a region in which the fiber reinjection approach significantly contributes to the evolution of fiber flocculation. The second flocculation regime, spanning $-7 < x/H < 5$, shows a constant flocculation rate, suggesting a fully developed state in which the fiber motion is independent of the reinjection approach before entering the diffuser. In the third regime, spanning $x/H \approx 5$ to $x/H \approx 19$, a sharp increase in the flocculation rate occurs due to the ballistic deflection of fibers, as reported in Andrić et al. (2016). As the mean flow velocity decreases through the diffuser section, the velocity gradient in the flow direction and the inertia of the fibers contribute to a velocity difference between the fibers and the flow. This relative velocity, coupled with the oriented hydrodynamic resistance tensor leads to a significant deviation of fiber trajectories from the flow streamlines (Andric et al., 2017). This phenomenon substantially increases fiber–fiber collisions and thus elevates the flocculation rate. Finally, downstream of $x/H = 19$, the suspension enters the fourth regime, where the flocculation rate stabilizes, indicating a nearly fully developed state of fiber flocculation.

The delayed rise in floc-production rate, observed near $x/H \approx 5$ rather than at $x = 0$, reflects the finite development length required for ballistic deflection to become significant, and for fibers to migrate laterally and attain the mutual orientations needed for collisions. These conditions only develop after particles acquire appreciable slip and reorient in the diffuser's decelerating flow. Fig. 5 shows that, for Cases 2–5, flocculation rates are broadly similar beyond $x/H \approx 5$, with comparable behavior in the regions $7 < x/H < 19$ and $19 < x/H < 36$. This observation indicates that ballistic deflection is the primary mechanism driving flocculation in the diffuser and that it is largely insensitive to the reinjection kinematics at the inlet.

Fig. 6 extends the parametric study by including two additional fiber densities of $\rho_{ref}/3$ and $\rho_{ref}/1000$ (approximately equal to the density of the carrier fluid, air), as well as varying reinjection approaches for these fibers. Case 2 is also shown in the graph to allow for direct comparisons with the cases presented in Fig. 5. The results indicate that floc formation is more pronounced for heavier fibers. Lighter fibers, due to their shorter response times, tend to align more closely with the flow, resulting in less deviation of fiber trajectories from the flow streamlines and lower fiber slip velocities. Consequently, they exhibit reduced floc formation. This behavior is particularly evident in the straight inlet duct and at the initial section of the diffuser. As can be seen in Fig. 6, fiber suspensions containing lighter fibers (Case 9–11) display a significantly lower flocculation rate and mass fraction ϕ_2 compared to suspensions with heavier fibers of density $\rho = 460\ \mathrm{kg/m^3}$. While random reinjection orientations enhance floc formation for both cases of fiber inertia (consistent with observations for the reference inertia in Fig. 5), comparing Cases 6 and 8 versus Cases 9 and 11, respectively, suggests that the reinjection approach has a greater impact on heavier fibers. A similar pattern to Cases 2–5 is observed in the development of floc formation along the diffuser for fibers with a density of $\rho = 460\ \mathrm{kg/m^3}$, with the exception of the far downstream region $x/H \geq 30$, where the flocculation rate is higher for fibers with a density of $\rho_{ref}/3$. Additionally, comparing cases containing lighter fibers (*i.e.,* Cases 9–11) with those involving heavier fibers, reveals that the diffuser has a more significant effect on the flocculation rate for fibers with higher inertia.

To assess whether aggregates with more than two fibers form, Fig. 7 reports the evolution of the three- and four-fiber mass fractions, (ϕ_3, ϕ_4), along the length of the diffuser for selected simulation cases. For reference, the evolution of ϕ_2 of Case 2 is included to facilitate direct comparison with the results presented in Figs. 5 and 6. The mass fractions of F_3 and F_4 flocs are negligible in the upstream straight channel

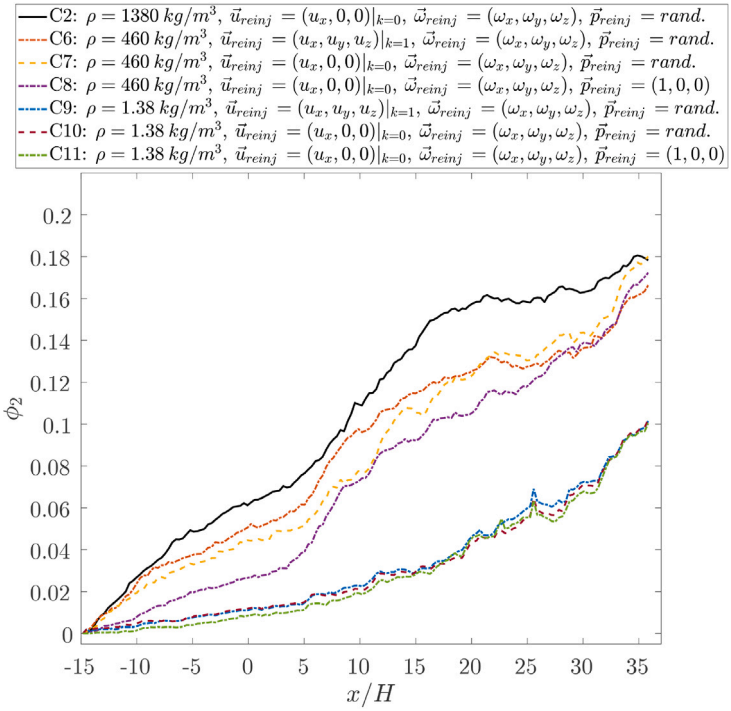

Fig. 6. Development of the mass fraction ϕ_2 of floc species F_2 along the diffuser length for different fiber reinjection approaches and fiber inertia.

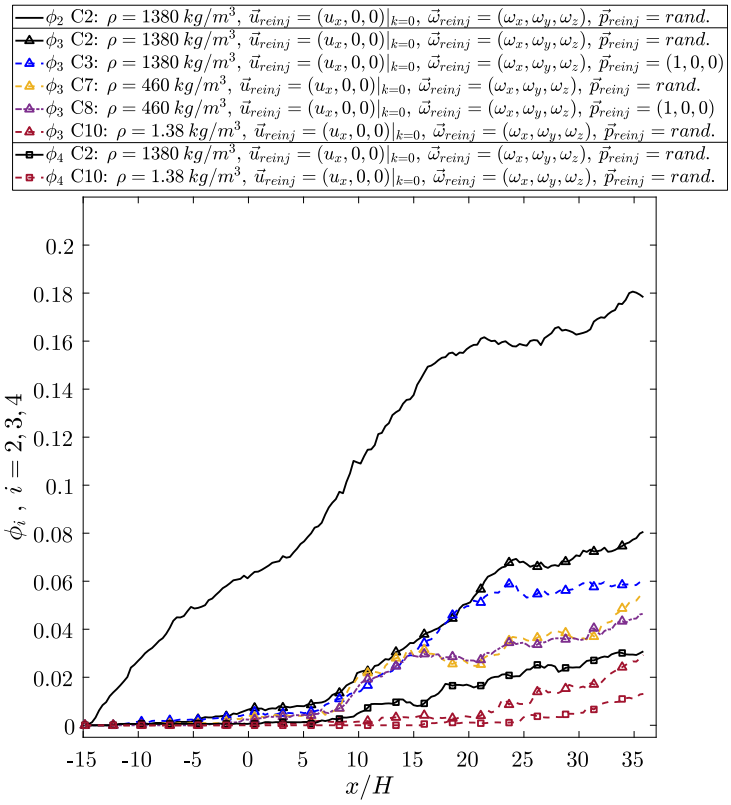

Fig. 7. Development of the mass fraction ϕ_3 and ϕ_4 along the length of the diffuser. The two-fiber floc (ϕ_2) curve of Case 2 is included in the plot as a reference.

and increase notably downstream of the diffuser entrance, reproducing relatively similar spatial behavior as previously reported for ϕ_2. As shown in Fig. 7, the mass fractions ϕ_3 exhibit an onset of growth at approximately the same streamwise location as ϕ_2 (roughly at $x/H \approx 5$) and attains most of its growth over the interval $5 < x/H < 20$. The evolution of ϕ_4 follows the same qualitative trend but with reduced magnitude and a modest downstream delay, which is consistent with the requirement that larger aggregates form by successive collision events, and lag lower-order ones in space. Variations in particle inertia and reinjection approach influence on both the amplitude and the

streamwise position of the ϕ_3 and ϕ_4 growth. In agreement with the trends observed for ϕ_2, heavier fibers develop larger values of ϕ_3 and ϕ_4 relative to lighter fibers, consistent with the enhancement of slip and ballistic deflection that accompanies increased inertia and that raises contact rates.

The comparatively low absolute level and delayed development of ϕ_4 both reflect the mechanistic nature of early-stage aggregation in the dilute regime and to the modeling limitation of the present study. Formation of three- and four-fiber aggregates requires multiple successive encounters within limited time windows; accordingly, such aggregates are less frequent and tend to appear further downstream than two-fiber flocs. Moreover, since the present numerical model treats contacting fibers as irreversibly sticking rigid bodies, the reported ϕ_3 and ϕ_4 should be interpreted primarily as indicators of collision propensity driven by hydrodynamic mechanisms (fiber slip and ballistic deflection), rather than as quantitative predictions of mature floc morphology in conditions where restructuring, sliding or breakage would be important. The correspondence between the spatial development of ϕ_2 (Figs. 5 and 6) and the higher-order mass fractions shown in Fig. 7 reinforces the conclusion that the same hydrodynamic drivers controlling pairwise encounters also govern the emergence of higher-order aggregates.

5.3. Fiber translational motion

Fig. 8 illustrates the relative trajectories of the centers of mass of 200 fibers from Cases 1–3, and 10. All trajectories are moved to start at $x/H = -15$ and $y/H = 0$, to visualize their relative deviation from the x-direction. Different colors are used for visualization purposes without carrying any specific information. A zoomed-in view, magnified by a factor of 2, is included at the bottom left corner of each plot, focusing on the straight inlet channel ($-15 < x/H < 0$). Note that some trajectories are truncated because the fibers either collided with the upper or lower walls or exited the domain through the outlet, in which case they were reinjected at the inlet according to the specified reinjection approach.

The zoomed-in views in Fig. 8 reveal that fibers with high inertia (Cases 1–3) tend to follow nearly straight trajectories, while the lighter fibers in Case 10, with their shorter response times, closely track the resolved flow fluctuations. A comparison of Cases 1–3 highlights the significant influence of the reinjection approach on the initial trajectories. The difference between Case 1 and Case 2 is the reinjection velocity. In Case 1, fibers are reinjected with velocities derived from the resolved flow at the center of mass of the fiber segments. In Case 2, fibers are assigned a velocity exclusively in the x-direction, corresponding to the time-averaged flow at the center of mass. Fibers characterized by higher inertia tend to retain their velocities. As a result, fibers in Case 1 exhibit immediate dispersion upon reinjection, whereas in Case 2, deviations from the x-direction occur further downstream. If the orientation happens to align with the reinjection velocity vector, the fibers may dart a far distance influenced mainly by the reinjection method. This phenomenon is evident when comparing Cases 2 and 3, where the dispersion in Case 3 is mitigated as the fiber orientation aligns with the reinjection velocity. It is important to note that none of the presently used reinjection approaches are perfectly accurate, hence the reinjection plane is positioned far upstream (*i.e.,* at $x/H = -15$) to allow the flocculation rate to reach a fully developed state before the fibers enter the diffuser region.

Given that the flow within the straight inflow channel predominantly aligns with the x-direction, any deviation of fiber trajectories from this axis may potentially elevate the fiber–fiber collisions. Consequently, Case 1, which displays the greatest deviation from the x-direction, also exhibits the highest flocculation rate and mass fraction ϕ_2 within the inlet channel. With a spatial lag from the diffuser entrance plane, the fibers perceive the effect of the decelerating flow and start to diffuse significantly. This phenomenon coincides with a sharp increase in the flocculation rate around $x/H \approx 5$ (see Figs. 5 and 6).

To quantify fiber spreading, the standard deviation of the transverse fiber center-of-mass position y conditioned on the streamwise location x, $\mathrm{Var}[y\,|\,x]$, is computed using an event-based estimator (Pishro-Nik, 2014). For each fiber trajectory, the transverse position $y_i(x)$ at which the trajectory first crossed a given streamwise bin centered at x is recorded. Across the $N_{\mathrm{cross}}(x)$ independent crossings in that bin the mean and variance are computed as

$$\bar{y}(x) = \frac{1}{N_{\mathrm{cross}}(x)} \sum_{i=1}^{N_{\mathrm{cross}}(x)} y_i(x), \tag{19}$$

$$\sigma^2_{\mathrm{cross}}(x) = \frac{1}{N_{\mathrm{cross}}(x)} \sum_{i=1}^{N_{\mathrm{cross}}(x)} \left(y_i(x) - \bar{y}(x)\right)^2. \tag{20}$$

The per-crossing standard deviation is used to ensure that each trajectory contributed equally to the statistics and to avoid residence-time bias. Bins with fewer than eight independent crossings are discarded (Pishro-Nik, 2014).

Fig. 9 shows the per-crossing standard deviation of the transverse fiber positions normalized by the inlet channel height, $\sigma_{\mathrm{cross}}(x)/H$, as a function of the streamwise coordinate (x/H) for the cases displayed in Fig. 8. All cases exhibit a consistent streamwise increase of lateral spreading from the reinjection plane up to $x/H \approx 25$. Upstream of the diffuser $(x/H < 0)$, Case 1 produced systematically larger transverse spreading than Case 10, Cases 2 and 3, the latter two showing negligible spreading (values close to the estimator's noise floor). Comparing these lateral-spread results with the flocculation development of Case 1 with Case 2 and 3 in Fig. 5 indicates that enhanced trajectory dispersion increases the probability of near encounters and collisions, which in turn yields higher floc formation over the same streamwise intervals.

As particles enter the diffuser the lateral spread grows rapidly, with the steepest increase beginning near $x/H \approx 5$. This behavior reproduces the qualitative features of the trajectory plots in Fig. 8 and matches the development length inferred from the flocculation analysis in Fig. 5, where the flocculation rate is observed to rise significantly. For $(10 < x/H < 20)$ the different cases display similar lateral dispersion, and a rough saturation of dispersion is reached beyond $x/H \approx 25$ at $\sigma_{\mathrm{cross}}(x)/H \approx 1$ in which fibers are distributed across approximately the inlet-height scale. These observations imply that (i) reinjection kinematics and particle inertia mainly affect the magnitude and early evolution of the lateral spread but not the overall qualitative trend, and (ii) within the parameter range investigated the dominant mechanism controlling transverse dispersion is the ballistic response of fibers to the large-scale flow deceleration in the diffuser.

To quantify the impact of wall-contact events on the suspended population, every reinjection event is classified as either a wall-contact or an outlet-crossing regardless of whether the fiber is an isolated fiber or part of a floc. The streamwise region $-15 < x/H < 36$ is partitioned into 320 equal bins; for each bin the number of reinjections attributed to wall contact is accumulated and normalized by the total number of reinjections across the entire fiber region, yielding both bin-wise and domain-integrated wall-hit fractions.

The domain-integrated wall-hit fractions are found to be approximately 16.7% for Case 1, 15.9% for Case 2, 15.8% for Case 3, and only $\approx 2.5\%$ for the low-inertia Case 11. These values reveal a clear dependence on particle inertia: lighter fibers closely follow streamlines and predominantly exit the domain through the outlet, whereas heavier fibers develop larger slip velocities inside the diffuser that produce stronger transverse motions and an elevated probability of wall contact. In the present very dilute regime, the per-particle collision probability per transit is already small ($\mathcal{O}(10^{-2} - 10^{-1})$). Therefore, localized concentration reductions caused by wall removal and reinjection alter the absolute collision probability only at the same order (*i.e.,* by roughly the reported wall-hit percentages) and do not change dominant mechanism enhancing local contact rates.

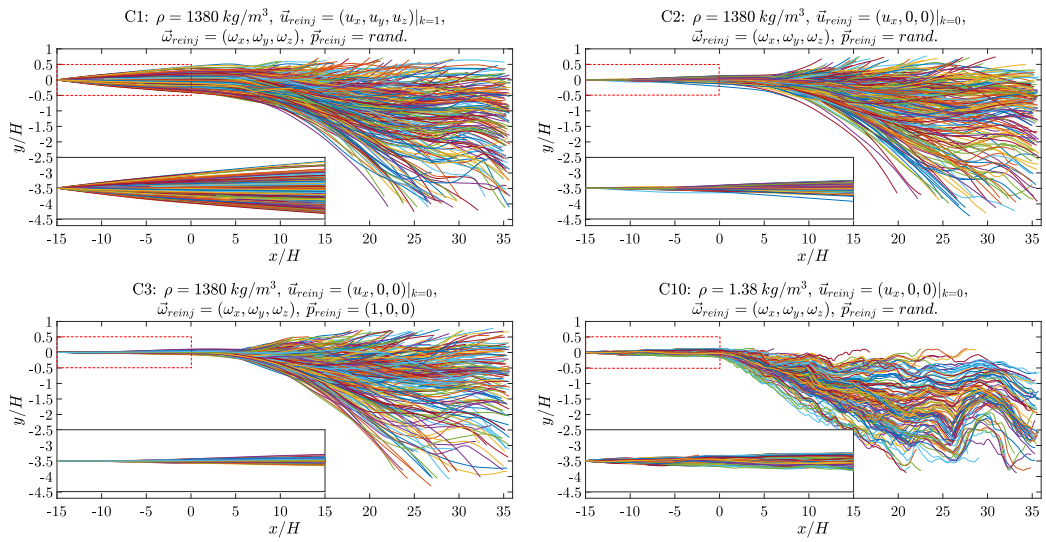

Fig. 8. Relative trajectories of fibers of Cases 1–3 and 10. Each line represents the trajectory of a single fiber. Colors distinguish different trajectories. Some trajectories end mid-domain as the analysis was stopped before fibers reached the walls. The streamwise axis is compressed to keep the panel compact and to highlight transverse and wall-distance variations.

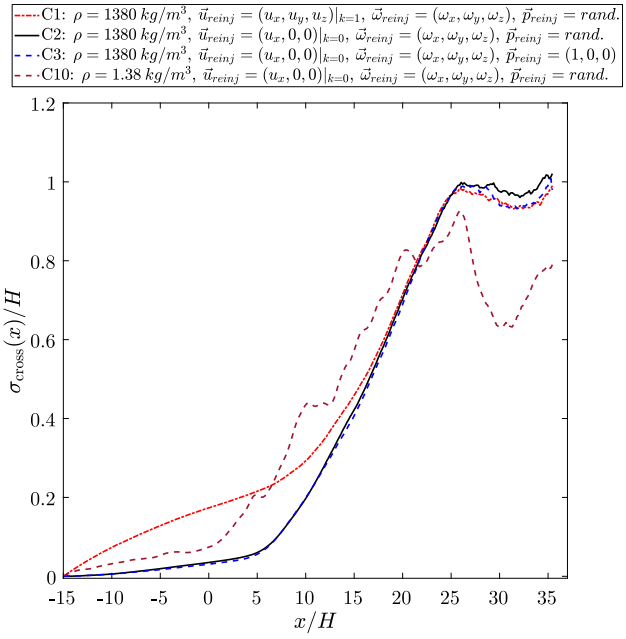

Fig. 9. Standard deviation of the transverse fiber positions normalized by inlet height along the length of the diffuser.

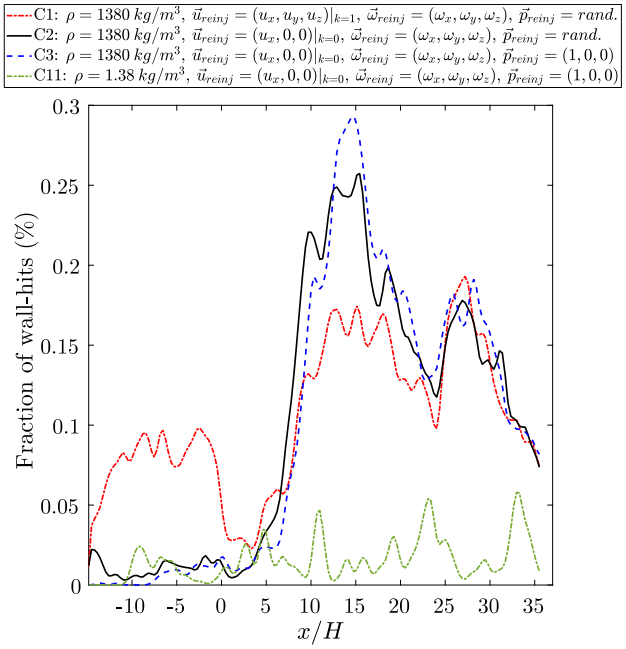

Fig. 10. Distribution of the wall-hit fraction along the length of the diffuser.

Fig. 10 shows the streamwise distribution of the wall-hit fraction. Upstream of the diffuser ($-15 < x/H < 0$), Case 1 – whose reinjected fibers include nonzero transverse velocity components – exhibits a higher wall-hit fraction than Cases 2 and 3, whose reinjections are constrained to the streamwise direction and therefore remain closely aligned with the mean flow. Inside the diffuser ($x/H > 0$), the wall-hit fraction increases notably for the heavier cases as inertia-driven (ballistic) deviations from the streamlines promote transverse motions and subsequent fiber-wall contacts; by contrast, the light-particle Case 11 maintains a low, approximately constant wall-hit fraction consistent with near-tracer behavior. Farther downstream the heavier cases converge toward similar wall-hit levels, indicating that particle inertia together with the diffuser geometry sets a comparable wall contact rate regardless of reinjection kinematics once the flow has fully expanded.

To further explore the influence of reinjection approaches and fiber inertia, the development of fiber slip velocity is also analyzed. The slip velocity vector is defined as ($\vec{u}_{slip} = \vec{v}_i - \dot{\vec{r}}_i$), where $\vec{v}_i$ represents the fluid velocity experienced by the fiber along its trajectory, and $\dot{\vec{r}}_i$) denotes the fiber's translational velocity. For this analysis, the fiber region ($-15 < x/H < 0$) is divided into 320 bins of uniform thickness along the x-direction, and the time-averaged magnitude of the slip velocity is calculated for fibers with centers of mass within each bin. Fig. 10 presents the normalized magnitude of the average fiber slip velocity, ($|\vec{u}_{slip}|/U_b$) along the length of the diffuser, where U_b is the fluid bulk velocity. The results reveal a strong correlation between slip velocity and fiber inertia. The lightest fibers considered ($\rho = 1.38$ kg/m^3) consistently exhibit a very low ratio of $|\vec{u}_{slip}|/U_b$ throughout the diffuser, regardless of their reinjection kinematics. For fibers with higher

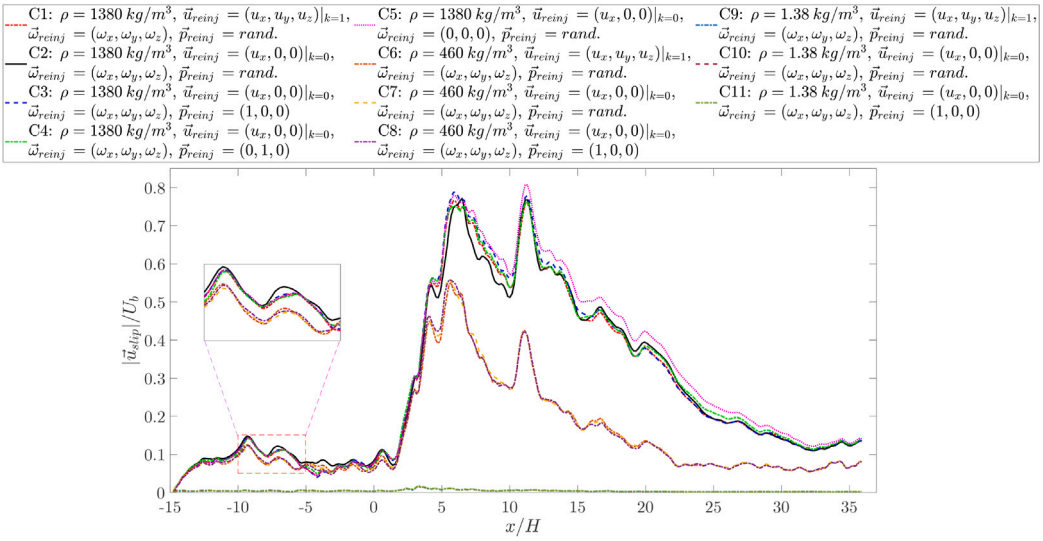

Fig. 11. Magnitude of average fiber slip velocity normalized by the fluid bulk velocity (U_b) along the length of the diffuser.

densities, the curves are grouped, indicating the influence of inertia on slip velocity behavior. The diffuser creates a localized deceleration: light fibers responded rapidly and therefore remained closely coupled to the fluid (small slip), whereas heavier fibers lagged and developed larger slip.

As illustrated in Fig. 11, the fibers in Cases 1–8 exhibit a similar evolution trend, again dependent on their inertia with minimal influence from their inlet kinematics. Upon reinjection, the fibers rapidly develop a relative velocity with respect to the carrying fluid, reaching a local peak at $x/H \approx -9$. Following this location, the slip velocity magnitude initially decreases and then stabilizes at a relatively constant value within the region $-5 < x/H < 0$. This observation aligns with the findings from Fig. 5, confirming the establishment of a fully developed flocculation regime prior to the fibers entering the diffuser. A sharp increase in the magnitude of the relative velocity between the fibers and the fluid occurs at $x/H = 2$. In Case 2, the averaged slip velocity increases rapidly from $0.06U_b$ at $x/H = 2$ to a maximum of $0.56U_b$ at $x/H = 6$. Similarly, in Case 1, it grows from $0.08U_b$ at $x/H = 6$ to a peak of $0.79U_b$ at $x/H = 6$. As previously discussed, this substantial increase in relative velocity, coupled with the oriented hydrodynamic resistance tensor, is the key mechanism driving fiber flocculation in the diffuser (Andrić et al., 2016). For fibers with moderate inertia ($\rho = 460\ \text{kg/m}^3$) in Cases 6–8, the magnitude of the fiber slip velocity generally decreases from $x/H = 6$ to the end of the diffuser section at $x/H = 21$, except for a localized peak at $x/H = 11$, after which the slip velocity stabilizes at approximately $0.6U_b$. This behavior can be attributed to the fact that fibers, after undergoing a ballistic deflection, make a transition into the viscosity-dominated regime of motion where their velocity approaches that of the flow. A similar trend is observed for fibers with higher inertia, although stabilization of their slip velocity occurs further downstream. A fully quantitative identification of the exact peak position would require a dedicated parametric study, which lies beyond the present study; nevertheless the L_{resp}-scaling may explain the observed peak qualitatively within the parameter range considered. For instance, for the cases with $\rho = 1380\ \text{kg/m}^3$ the observed local maxima at $x/H \approx 5.1,\ 11,\ 16,\ 20$ lay close to $1, 2, 3, 4 \times L_{\text{resp}}$, supporting a relaxation/overshoot interpretation in which particles required $\mathcal{O}(\tau_p)$ to adjust to diffuser deceleration.

5.4. Fiber alignment

The alignment of the fibers can be characterized by the orientation of the fiber's orientation direction ($\vec{p}$) relative to any direction of interest. It can be quantified using the cosine function, $\cos\psi$, where ψ represents the angle between the fiber principal axis and the direction of interest. For example, a value of $|\cos\psi| \approx 1$ indicates perfect alignment (parallel), while $\cos(\psi) = 0$ indicates a perpendicular alignment to the direction of interest. The alignment trends are further analyzed using the probability density function (PDF) of the cosine function $\cos\psi$. The PDF is computed using $f(\phi) = N_\phi/N$, where $\phi = \xi_i$ and ξ_i is the ith variable of interest (*e.g.,* cosine function of a specific angle between fiber principal axis and x-direction), N is the total number of samples used, N_ϕ is the number of fibers that fall within a given bin $[\phi, \phi + \Delta\phi]$ with a bin size of $\Delta\phi = (\phi_{max} - \phi_{min})/N_B$ and N_B is the number of bins (Njobuenwu and Fairweather, 2016). The normalization condition $\sum_{i=1}^{N_B} f\left(\phi_i\right) = 1$ ensures the PDF integrates to unity.

The alignment of the fibers with respect to the x-axis is studied in Fig. 12. Fig. 12(A) shows the evolution of fiber alignment, quantified by the average absolute value of $\cos\alpha$, where α is the angle between the fiber's principal axis and the streamwise direction (x). This value is averaged within each of 320 bins of uniform thickness along the streamwise direction of the fiber region $-15 < x/H < 36$. Fig. 12(B) presents the probability density function (PDF) of the direction cosine. It is important to note that the statistics presented in Fig. 12(B) are sampled exclusively from fibers traveling within the straight inflow channel $-15 < x/H < 0$.

In Fig. 12(A), light fibers ($\rho = 1.38\ \text{kg/m}^3$) reinjected along the x-axis (Case 11) maintain a strong alignment with the streamwise direction throughout the horizontal inlet channel ($-15 < x/H < 0$), as also evidenced in Fig. 12(B), where the PDF of the average direction cosine of the angle α exhibits a sharp peak at $\cos\alpha \approx 1$ with minimal distribution across other orientations. This strong alignment indicates that light fibers in Case 11 predominantly retain their orientation, experiencing limited reorientation as they move downstream. The initial alignment with the streamwise flow, combined with low inertia, enables these fibers to stay oriented along the flow direction with little resistance, reducing collisions and contributing to low flocculation, as previously observed in Fig. 6. Light fibers reinjected with random orientations (*e.g.,* Cases 9 and 10) demonstrate a tendency to reorient along the flow, gradually shifting from $\cos\alpha \approx 0.51$ at $x/H \approx -15$ to $\cos\alpha \approx 0.75$ at $x/H \approx 0$ (Fig. 12(A)). The PDF of the average direction cosine in Fig. 12(B) further illustrates this reorientation trend, showing two peaks at $\cos\alpha \approx -1$ and $\cos\alpha \approx 1$ alongside flatter regions, indicating incomplete alignment across the population by the time of measurement, and suggesting that some randomness persists. This broader orientation distribution fosters more frequent interactions

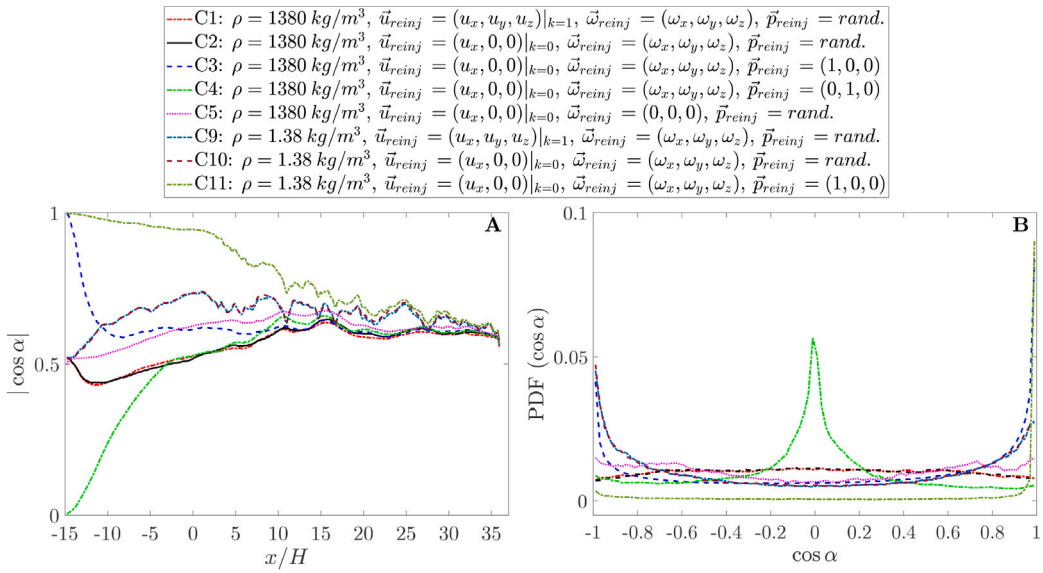

Fig. 12. (A) Development of the average direction cosine of the angle α between the fiber principal axis ($\vec{p}$) and the global x-axis along the diffuser length, (B) Probability density function of the direction cosine, PDF($\cos\alpha$) of the angle α between the fiber principal axis and the x-axis for fibers traveling within the inlet channel $-15 < x/H < 0$.

and collisions among fibers, thus increasing flocculation likelihood, as seen for Cases 9 and 10 in Fig. 6.

In Fig. 12(B), Case 3 which involves heavier fibers with the reference density $\rho = 1380\ \mathrm{kg/m^3}$ reinjected similarly to Case 11, exhibits two peaks at $\cos\alpha \approx -1$ and $\cos\alpha \approx 1$, indicating a strong parallel alignment with the streamwise direction. For Case 4, where heavy fibers are initially oriented perpendicular to the streamwise direction, the PDF shows a peak at $\cos\alpha \approx 0$, indicating a strong preference for perpendicular alignment. Fig. 12(A) illustrates that both Case 3 and Case 4 show a shift toward random alignment by the diffuser entrance, potentially influenced by several factors. First, heavy fibers, owing to their higher momentum, do not immediately respond to flow direction changes, leading to oscillations around the flow direction or transient random orientations as they gradually adjust. Additionally, shear-induced rotation near channel walls and high-gradient regions may apply asymmetric forces across fibers, which can disrupt initial alignments and promote more randomized orientations. In Fig. 12(B), for reference fibers with randomly set initial orientations (Cases 1, 2, and 5), the PDF of $\cos\alpha$ show relatively flat profiles, varying by approximately 3%, indicating a random distribution of fibers orientation with no clear preferential alignment within the inflow channel. As noted earlier, this broader distribution of orientations increases the likelihood of fiber-path crossing and interactions, contributing to higher amount of flocs formed in cases where the fiber orientation is randomly set upon reinjection compared to cases initially aligned along the x or y-axis.

Interestingly, Fig. 12(A) shows that the average fiber orientation relative to the streamwise direction converges to $|\cos\alpha| \approx 0.6$ at the end of the diffuser, regardless of fiber inertia or reinjection kinematics. This value closely matches the theoretical expectation for randomly oriented fibers, where the average absolute value of cosine is $|\cos\alpha| = \frac{2}{\pi} \approx 0.63$. The observed alignment suggests that fiber orientations are largely randomized by strong velocity gradients, turbulence and flow instabilities, with the slight deviation from the theoretical value likely due to flow-induced biases or directional preferences within the diffuser.

Fiber inertia strongly influences the evolution of fiber alignment. Fig. 12(A) shows that heavy fibers exhibit smoother orientation curves, reflecting more stable orientations and synchronous flipping at specific locations. Their greater momentum and resistance to rapid directional changes result in less frequent orientation adjustments compared to lighter fibers, highlighting that fiber inertia strongly affect the timescale of reorientation. Regarding the impact of reinjection linear and angular fiber velocity on fiber alignment, a comparison between the results from Cases 1 and 2 for heavy fibers ($\rho = 1380\ \mathrm{kg/m^3}$), and Cases 9 and 10 for light fibers ($\rho = 1.38\ \mathrm{kg/m^3}$) indicates that changes in linear velocity have minimal impact on fiber alignment with respect to the x-axis (see Fig. 12(A)). However, varying the reinjection angular velocity appears to significantly affect the orientation evolution, as highlighted by the results from Case 5.

6. Conclusions

The present study investigated the flocculation behavior of rigid fibers suspended in flow through a diffuser, focusing on the effects of fiber reinjection approaches and fiber inertia. The motion of the fibers was numerically simulated using the rod-chain model for rigid fibers, as used by Lindström and Uesaka (Lindström and Uesaka, 2007) and Andrić et al. (2013). Large Eddy Simulation (LES) was applied to resolve the detailed flow dynamics and fiber-flow interactions. Additionally, short-range attractive forces responsible for floc formation were considered.

The analysis of the mass fraction of two-fiber flocs identified four distinct growth flocculation regimes, each characterized by different growth rates. The first regime, from $x/H = -15$ to $x/H \approx -7$, is marked by an initial rapid rise in floc formation, followed by a more gradual nearly linear growth. The reinjection approach plays a key role in the evolution of the flocculation process in this region. In the second regime, spanning from $x/H = -7$ to $x/H = 5$, flocculation proceeds at a constant rate across all cases, indicating that fiber motion has reached a fully developed state, and it is now independent of the reinjection approach. The third regime, from $x/H = 5$ to $x/H = 19$, exhibits a sharp increase in the flocculation rate due to the ballistic deflection of the fibers. As the flow velocity decreases in the diffuser, the velocity difference between the fibers and the flow, combined with the influence of hydrodynamic resistance tensor, causes significant deflection of fiber trajectories. This ballistic deflection leads to increased fiber–fiber collisions, enhancing flocculation, and emerges as the dominant mechanism driving flocculation within the diffuser. Finally, in the fourth regime, downstream of $x/H = 19$, flocculation approaches a nearly fully developed state.

The degree of flocculation in the straight inflow channel is highest when fibers are reinjected with random orientations and their linear velocity components are derived from the three-dimensional instantaneous flow field. When fibers are reinjected with only the streamwise component of the time-averaged velocity, flocculation decreases, and it is further suppressed when fibers are aligned with the flow direction upon reinjection.

The impact of fiber inertia on flocculation behavior was also examined, revealing that denser fibers exhibit greater flocculation tendencies. Lighter fibers, in contrast, align more closely with streamlines, experience lower slip velocities, and undergo fewer collisions, leading to reduced floc formation. Additionally, the reinjection approach plays a more pronounced role in flocculation dynamics for heavier fibers, demonstrating that the interplay between fiber inertia and reinjection kinematics significantly influences floc formation and growth.

The analysis of fiber alignment within the diffuser provided key insights. Regardless of fiber inertia or reinjection kinematics, the orientation of fibers with respect to the streamwise direction converged to a common value by the outlet duct, suggesting that turbulence within the diffuser randomizes fiber orientation, resulting in a relatively uniform alignment downstream. However, heavier fibers exhibited less reorientation compared to lighter fibers due to their higher momentum and greater resistance to flow-induced rotation, indicating that inertia influences the timescale of fiber reorientation.

To place the reinjection study in context, it is emphasized that reinjection is a modeling assumption and that quantitative inlet statistics for reinjected fibers are not available from measurements. A reference reinjection condition (Case 2) is therefore adopted to represent a fully developed, predominantly streamwise approach flow in a statistically unbiased manner. The remaining prescriptions (*e.g.,* retaining additional translational velocity components or imposing aligned orientations) are treated as sensitivity tests to bracket the influence of non-equilibrium inlet kinematics on the onset of aggregation near the diffuser entrance. Establishing reinjection conditions in a predictive, device-specific sense would require dedicated experiments and/or higher-fidelity two-way coupled simulations, which is beyond the scope of the present work.

Despite offering valuable insights into rigid-fiber flocculation in an asymmetric diffuser, the present study has several limitations. We model irreversible sticking and treat formed flocs as rigid bodies, with focus on early-stage, predominantly two-fiber collisions in a dilute regime; consequently, floc deformation, bond breakage, internal rearrangement and the downstream persistence of large multi-fiber aggregates are likely underestimated. We also assume a fixed fiber length and omit contact physics such as friction and short-range repulsion, while only dilute suspensions are considered. These simplifications limit the applicability of our results and motivate future extensions to finite-strength bonds, deformable flocs, variable fiber lengths and higher volume fractions (with two-/four-way coupling).

CRediT authorship contribution statement

MohammadJavad Norouzi: Writing – review & editing, Writing – original draft, Visualization, Validation, Supervision, Software, Resources, Project administration, Methodology, Investigation, Funding acquisition, Formal analysis, Data curation, Conceptualization. **Jelena Andrić:** Writing – review & editing, Visualization, Validation, Supervision, Software, Project administration, Methodology, Investigation, Formal analysis, Data curation, Conceptualization. **Anton Vernet:** Writing – review & editing, Supervision, Resources, Project administration, Investigation, Funding acquisition, Conceptualization. **Jordi Pallares:** Writing – review & editing, Supervision, Resources, Project administration, Investigation, Funding acquisition, Conceptualization. **Håkan Nilsson:** Writing – review & editing, Visualization, Validation, Supervision, Software, Project administration, Methodology, Investigation, Formal analysis, Data curation, Conceptualization.

Declaration of competing interest

The authors declare that they have no known competing financial interests or personal relationships that could have appeared to influence the work reported in this paper.

Acknowledgments

This project has received funding from the European Union's Horizon 2020 research and innovation programme under the Marie Skłodowska-Curie grant agreement No. 713679 and from the Universitat Rovira i Virgili (URV). This work has been funded by the Spanish Ministerio de Ciencia, Innovación *y* Universidades/Agencia Estatal de Investigación/FEDER, under projects PID2020-113303GB-C21 and PID2023-146648NB-C21 and by Generalitat de Catalunya - AGAUR, under project 2021SGR00732. A part of the work has been performed under the Project HPC-EUROPA3 (INFRAIA-2016-1-730897), with the support of the EC Research Innovation Action under the H2020 Programme; in particular, the authors gratefully acknowledge the support of Dr. Andreas Ruopp, Department of Numerical Methods & Libraries of the High Performance Computing Center Stuttgart (HLRS), and the computer resources and technical support provided by HLRS High Performance Computing Center Stuttgart.

Data availability

Data will be made available on request.

References

Andrić, J., Fredriksson, S.T., Lindström, S.B., Sasic, S., Nilsson, H., 2013. A study of a flexible fiber model and its behavior in DNS of turbulent channel flow. Acta Mech. 224 (10), 2359–2374.

Andrić, J., Lindström, S., Sasic, S., Nilsson, H., 2016. Ballistic deflection of fibres in decelerating flow. Int. J. Multiph. Flow 85, 57–66.

Andric, J.S., Lindström, S.B., Sasic, S.M., Nilsson, H., 2017. Particle-level simulations of flocculation in a fiber suspension flowing through a diffuser. In: Thermal Science. Vol. 21.

Ardekani, M.N., Brandt, L., 2019. Turbulence modulation in channel flow of finite-size spheroidal particles. J. Fluid Mech. 859, 887–901.

Ardekani, M.N., Sardina, G., Brandt, L., Karp-Boss, L., Bearon, R., Variano, E., 2017. Sedimentation of inertia-less prolate spheroids in homogenous isotropic turbulence with application to non-motile phytoplankton. J. Fluid Mech. 831, 655–674.

Buice, C.U., Eaton, J.K., 2000. Experimental investigation of flow through an asymmetric plane diffuser: (data bank contribution)1. J. Fluids Eng. 122 (2), 433–435. http://dx.doi.org/10.1115/1.483278.

Challabotla, N.R., Zhao, L., Andersson, H.I., 2015. Orientation and rotation of inertial disk particles in wall turbulence. J. Fluid Mech. 766, R2.

Dotto, D., Marchioli, C., 2019. Orientation, distribution, and deformation of inertial flexible fibers in turbulent channel flow. Acta Mech. 230, 597–621.

Elghobashi, S., 1994. On predicting particle-laden turbulent flows. Appl. Sci. Res. 52 (4), 309–329.

Hämäläinen, J., Lindström, S.B., Hämäläinen, T., Niskanen, H., 2011. Papermaking fibre-suspension flow simulations at multiple scales. J. Engrg. Math. 71, 55–79.

Hinch, E., Leal, L., 1979. Rotation of small non-axisymmetric particles in a simple shear flow. J. Fluid Mech. 92 (3), 591–607.

Horiuti, K., 1985. Large eddy simulation of turbulent channel flow by one-equation modeling. J. Phys. Soc. Japan 54 (8), 2855–2865.

Jafari, A., Zamankhan, P., Mousavi, S.M., Henttinen, K., 2006. Multiscale modeling of fluid turbulence and flocculation in fiber suspensions. J. Appl. Phys. 100 (3).

Jeffery, G.B., 1922. The motion of ellipsoidal particles immersed in a viscous fluid. Proc. R. Soc. Lond. Ser. A, Contain. Pap. A Math. Phys. Character 102 (715), 161–179.

Kajishima, T., Nomachi, T., 2006. One-equation subgrid scale model using dynamic procedure for the energy production. J. Appl. Mech. 73 (3), 368–373. http://dx.doi.org/10.1115/1.2164509.

Kaltenbach, H.-J., Fatica, M., Mittal, R., Lund, T., Moin, P., 1999. Study of flow in a planar asymmetric diffuser using large-eddy simulation. J. Fluid Mech. 390, 151–185.

Kerekes, R.J., Schell, C.J., 1995. Effects of fiber length and coarseness on pulp flocculation. Tappi J.–(USA).

Kim, S., Karrila, S.J., 2013. Microhydrodynamics: Principles and Selected Applications. Courier Corporation, Mineola, New York.

Koch, D.L., Shaqfeh, E.S., 1989. The instability of a dispersion of sedimenting spheroids. J. Fluid Mech. 209, 521–542.
Lindström, S.B., Uesaka, T., 2007. Simulation of the motion of flexible fibers in viscous fluid flow. Phys. Fluids 19 (11).
Locsei, J., Pedley, T., 2009. Run and tumble chemotaxis in a shear flow: the effect of temporal comparisons, persistence, rotational diffusion, and cell shape. Bull. Math. Biol. 71, 1089–1116.
Lopez, D., Guazzelli, E., 2017. Inertial effects on fibers settling in a vortical flow. Phys. Rev. Fluids 2 (2), 024306.
Lovecchio, S., Marchioli, C., Soldati, A., 2013. Time persistence of floating-particle clusters in free-surface turbulence. Phys. Rev. E 88 (3), 033003.
Lovecchio, S., Zonta, F., Marchioli, C., Soldati, A., 2017. Thermal stratification hinders gyrotactic micro-organism rising in free-surface turbulence. Phys. Fluids 29 (5).
Lundell, F., Söderberg, L.D., Alfredsson, P.H., 2011. Fluid mechanics of papermaking. Annu. Rev. Fluid Mech. 43, 195–217.
Marchioli, C., Fantoni, M., Soldati, A., 2010. Orientation, distribution, and deposition of elongated, inertial fibers in turbulent channel flow. Phys. Fluids 22 (3).
Marchioli, C., Soldati, A., 2013. Rotation statistics of fibers in wall shear turbulence. Acta Mech. 224 (10), 2311–2329.
Martínez, M., Vernet, A., Pallares, J., 2020. Collisions and caustics frequencies of long flexible fibers in two-dimensional flow fields. Acta Mech. 231, 2979–2987.
Meyer, C.R., Byron, M.L., Variano, E.A., 2013. Rotational diffusion of particles in turbulence. Limnol. Ocean.: Fluids Environ. 3 (1), 89–102.
Ni, R., Ouellette, N.T., Voth, G.A., 2014. Alignment of vorticity and rods with Lagrangian fluid stretching in turbulence. J. Fluid Mech. 743, R3.
Njobuenwu, D.O., Fairweather, M., 2016. Simulation of inertial fibre orientation in turbulent flow. Phys. Fluids 28 (6).
Norouzi, M., Andric, J., Vernet, A., Pallares, J., 2022. Shape evolution of long flexible fibers in viscous flows. Acta Mech. 233 (5), 2077–2091.
Obi, S., Aoki, K., Masuda, S., 1993. Experimental and computational study of turbulent separating flow in an asymmetric plane diffuser. In: Ninth Symposium on Turbulent Shear Flows. Vol. 305, pp. 305–312.
Okamoto, M., Shima, N., 1999. Investigation for the one-eaquation-type subgrid model with eddy-viscosity expression including the shear-damping effect. JSME Int. J. Ser. B Fluids Therm. Eng. 42 (2), 154–161.
Olivieri, S., Mazzino, A., Rosti, M.E., 2022. On the fully coupled dynamics of flexible fibres dispersed in modulated turbulence. J. Fluid Mech. 946, A34.
Parsa, S., Calzavarini, E., Toschi, F., Voth, G.A., 2012. Rotation rate of rods in turbulent fluid flow. Phys. Rev. Lett. 109 (13), 134501.
Pishro-Nik, H., 2014. Introduction to Probability, Statistics, and Random Processes. Kappa Research, LLC Blue Bell, PA, USA.
Saintillan, D., Shelley, M.J., 2007. Orientational order and instabilities in suspensions of self-locomoting rods. Phys. Rev. Lett. 99 (5), 058102.
Schmid, C.F., Switzer, L.H., Klingenberg, D.J., 2000. Simulations of fiber flocculation: Effects of fiber properties and interfiber friction. J. Rheol. 44 (4), 781–809.
Sherwood, S.C., Phillips, V.T., Wettlaufer, J., 2006. Small ice crystals and the climatology of lightning. Geophys. Res. Lett. 33 (5).
Switzer, L.H., Klingenberg, D.J., 2004. Flocculation in simulations of sheared fiber suspensions. Int. J. Multiph. Flow 30 (1), 67–87.
Switzer III, L.H., Klingenberg, D.J., 2003. Rheology of sheared flexible fiber suspensions via fiber-level simulations. J. Rheol. 47 (3), 759–778.
Tang, H., Lei, Y., Li, X., Fu, Y., 2019. Large-eddy simulation of an asymmetric plane diffuser: Comparison of different subgrid scale models. Symmetry 11 (11), 1337.
Tom, J., Bragg, A.D., 2019. Multiscale preferential sweeping of particles settling in turbulence. J. Fluid Mech. 871, 244–270.
Toschi, F., Bodenschatz, E., 2009. Lagrangian properties of particles in turbulence. Annu. Rev. Fluid Mech. 41, 375–404.
Vega, C., Lago, S., 1994. A fast algorithm to evaluate the shortest distance between rods. Comput. Chem. 18 (1), 55–59.
Voth, G.A., Soldati, A., 2017. Anisotropic particles in turbulence. Annu. Rev. Fluid Mech. 49, 249–276.
Weller, H.G., Tabor, G., Jasak, H., Fureby, C., 1998. A tensorial approach to computational continuum mechanics using object-oriented techniques. Comput. Phys. 12 (6), 620–631.
Yoshizawa, A., Horiuti, K., 1985. A statistically-derived subgrid-scale kinetic energy model for the large-eddy simulation of turbulent flows. J. Phys. Soc. Japan 54 (8), 2834–2839.
Zhao, L., Andersson, H.I., 2020. Why spheroids orient preferentially in near-wall turbulence–CORRIGENDUM. J. Fluid Mech. 887, E1.
Zhao, L., Challabotla, N.R., Andersson, H.I., Variano, E.A., 2019a. Mapping spheroid rotation modes in turbulent channel flow: effects of shear, turbulence and particle inertia. J. Fluid Mech. 876, 19–54.
Zhao, F., George, W., van Wachem, B.G., 2015. Four-way coupled simulations of small particles in turbulent channel flow: The effects of particle shape and Stokes number. Phys. Fluids 27 (8).
Zhao, L., Gustavsson, K., Ni, R., Kramel, S., Voth, G., Andersson, H., Mehlig, B., 2019b. Passive directors in turbulence. Phys. Rev. Fluids 4 (5), 054602.
Zhao, L., Marchioli, C., Andersson, H.I., 2014. Slip velocity of rigid fibers in turbulent channel flow. Phys. Fluids 26 (6).